ChemPubSoc Europe

DOI: 10.1002/celc.201600215

CHEMELECTROCHEM Communications

Self-Supporting and Binder-Free Anode Film Composed of Beaded Stream-Like $Li_4Ti_5O_{12}$ Nanoparticles for High-Performance Lithium-Ion Batteries

Kaifu Huo,*[a] Xingxing Li,[b] Biao Gao,[b] Lei Wang,[a] Qingwei Li,[a] Xiang Peng,[c] Xuming Zhang,[b, c] Jijiang Fu,[b] and Paul K. Chu*[c]

A self-supporting film composed of arrays of $Li_4Ti_5O_{12}$ (LTO) nanoparticles (NPs) prepared through chemical lithiation of anodic TiO_2 nanotube arrays and calcination in air is used as a high-performance binder-free anode in lithium-ion batteries (LIBs). The LTO nanoparticles formed in situ are closely connected along the axial direction of the pristine TiO_2 nanotubes, forming a beaded stream-like structure. The self-supporting NPs film has a large tap density and overall packing factor, and the three-dimensional (3D) network of NPs increases the electroactive interface, facilitating transfer of Li^+ and enhancing the intercalation kinetics during charging/discharging. The LTO electrode with excellent mechanical flexibility and robustness has a volumetric capacity of 304 mAh cm^{-3} at a current density of 50 mA cm^{-3} as well as a high rate capability of 208 mAh cm^{-3} at 5000 mA cm^{-3}. After undergoing 500 cycles at a high current density of 1250 mA cm^{-3}, 91.4% of the capacity is retained, demonstrating high reversibility and cycling stability of the binder-free LTO NPs film electrode in LIBs.

Rechargeable lithium-ion batteries (LIBs) are popular power sources in consumer electronics and electrical/hybrid vehicles.[1–4] However, current LIBs based on graphite anode materials generally suffer from limitations such as small power density and safety issues. The low operating potential of graphite anodes (below 0.2 V vs. Li/Li^+) frequently leads to the formation of a solid electrolyte interface (SEI) film and even dendritic lithium deposition on the anode surface at overcharged states, raising safety concerns.[4–6] Furthermore, graphite anodes generally deliver poor rate performance, owing to the intrinsically small Li^+ diffusion coefficient. As an alternative to graphitic carbon, spinel $Li_4Ti_5O_{12}$ (LTO) has several inherent advantages.[3,4] Firstly, LTO exhibits a flat and stable operating potential around 1.5 V (vs. Li/Li^+), which makes it safer by avoiding reduction of electrolytes and Li-metal deposition. Secondly, as a zero-strain insertion material, spinel LTO can accommodate up to three lithium ions per formula unit (theoretical capacity of 175 mAh g^{-1}) with negligible volume change during charging and discharging, and so a long cycle life is possible.[4,5,7,8] Lastly, titanium is quite abundant and LTO is, therefore, cost-effective.

Despite these perceived advantages, the low electron conductivity ($<10^{-13}$ S cm^{-1}) and small Li^+ diffusion coefficient (10^{-9}–10^{-13} cm^2 s^{-1}) of LTO result in a poor rate capability and severe polarization, especially at large current densities.[8–10] A promising strategy to improve the rate performance of LTO is to construct proper nanostructures to reduce the transport distance for both ions and electrons and provide a large active surface for the electrochemical reactions.[11–13] Various nanostructured LTO materials, such as nanoparticles (NPs), nanofibers, nanosheets, and hierarchically porous microspheres with improved kinetic performance, have been produced.[3,14–16] Powder-like LTO nanomaterials generally need to be mixed with a polymeric binder and carbon black before being pressed into a current collector for assembly into a battery cell. However, addition of the inactive and insulating binder inevitably increases the weight of electrodes and produces undesirable interfaces, compromising the energy-storage capacity. In this context, binder-free anodes, in which active materials are fabricated directly on a current collector, can overcome these drawbacks and deliver better electrochemical performances.[8,17–19] Recently, hydrogenated LTO nanowires[17] and LTO nanosheet arrays[8] prepared on Ti in situ have been demonstrated as high-performance anodes with improved rate capability. However, to the best of our knowledge, self-supporting and binder-free films containing LTO NPs fabricated directly on a current-collecting substrate with robust mechanical stability have not been reported, although this type of film offers unique advantages in terms of electrode manufacturing and electrochemical performance. Firstly, the three-dimensional (3D) network of NPs increases the electroactive interface, facilitating transfer of Li^+, thereby enhancing the intercalation kinetics during charging/discharging and a producing high capacity and rate capability. Secondly, the dense 3D NPs have a large tap density and overall packing factor, consequently yielding a large battery capacity/weight ratio as well as gravi-

[a] Prof. K. Huo, L. Wang, Q. Li
Wuhan National Laboratory for Optoelectronics (WNLO) and
School of Optical and Electronic Information
Huazhong University of Science and Technology
Wuhan 430074 (China)
E-mail: kfhuo@hust.edu.cn

[b] X. Li, B. Gao, Dr. X. Zhang, Prof. J. Fu
The State Key Laboratory of Refractories and Metallurgy
Wuhan University of Science and Technology
Wuhan 430081 (China)

[c] X. Peng, Dr. X. Zhang, Prof. P. K. Chu
Department of Physics and Materials Science
City University of Hong Kong
Tat Chee Avenue, Kowloon, Hong Kong (China)
E-mail: paul.chu@cityu.edu.hk

Supporting Information and the ORCID identification number(s) for the author(s) of this article can be found under http://dx.doi.org/10.1002/celc.201600215.

metric and volumetric capacity. Thirdly, the fabrication process can be simplified by connecting the active NPs to the current-collecting substrate. In addition, the film composed of LTO NPs on conducting Ti has excellent mechanical flexibility, which bodes well for applications in flexible energy-storage devices.

Herein, a self-supporting and binder-free film consisting of LTO NPs is fabricated to serve as a high-performance anode in LIBs. The film is prepared by chemical lithiation of anodized titanium-oxide nanotube arrays (TiO_2 NTAs) directly grown on a Ti foil with subsequent calcination in air. The 1D TiO_2 nanotubes are transformed into beaded stream-like LTO NPs (BLTO NPs), which are interconnected along the primitive axial direction of the TiO_2 NTAs, producing 1D beaded stream-like nanowires (Scheme 1).

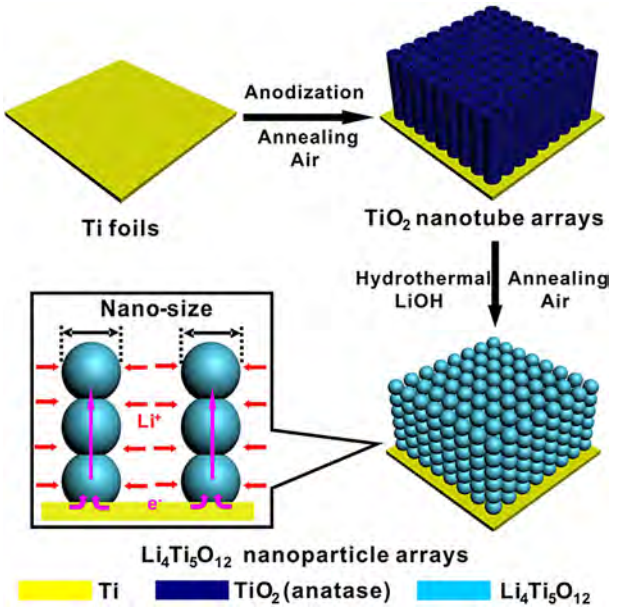

Scheme 1. Schematic diagram illustrating the fabrication of self-supporting BLTO NPs.

An amorphous TiO_2 NTAs film is prepared on a Ti foil through electrochemical anodic oxidation in ethylene glycol containing 0.5 wt% ammonium fluoride (NH_4F), 5 vol% distilled water, and 5 vol% methanol (CH_3OH). The anodized amorphous TiO_2 NTAs are annealed at 450 °C for 3 h in air to produce anatase-TiO_2 NTAs, which are further hydrothermally treated in LiOH and annealed in air to produce the BLTO NPs film. Owing to the good electrical contact between the LTO NPs and Ti current collector, there is effective interparticle charge transfer between them. In addition, the self-supporting 3D film has a porous structure and high electrode/electrolyte contact area to facilitate electrolyte diffusion as well as ion and electron transfer. As a result, the BLTO NPs anode attains a volumetric capacity of 304 mAh cm^{-3} at a current density of 50 mA cm^{-3} as well as a high rate capability of 208 mAh cm^{-3} at 5000 mA cm^{-3}. After undergoing 500 cycles at a current density of 1250 mA cm^{-3}, 91.4% of the capacity is retained, indicating excellent cycle stability.

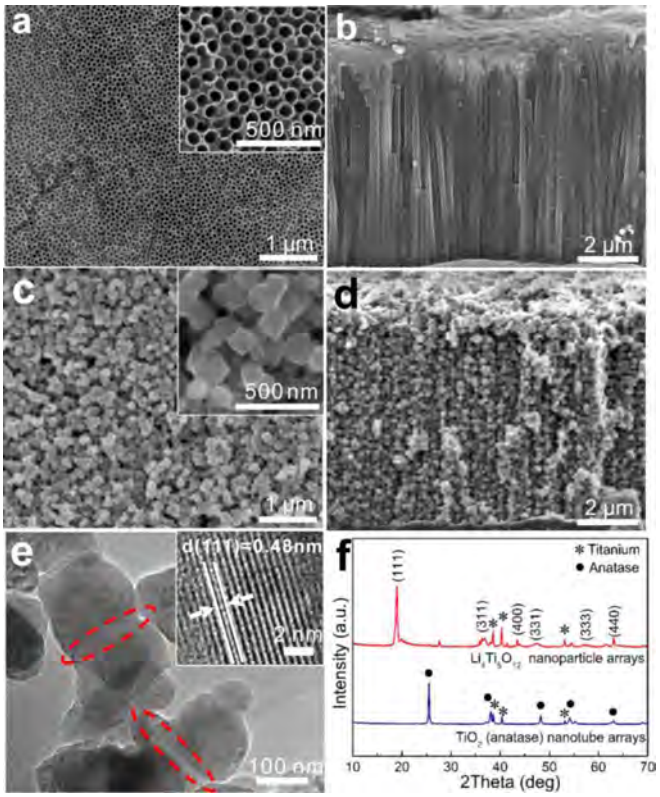

Figure 1. Top- and side-view SEM images of a, b) TiO_2 NTAs and c, d) BLTO NPs. The insets in (a, c) are the corresponding high-magnification SEM images. e) TEM images of BLTO NPs (joints marked by red dotted oval line). The inset in (e) is the corresponding HR-TEM image. f) XRD patterns of the TO_2 NTAs and BLTO NPs.

Figure 1a depicts the top-view scanning electron microscopy (SEM) image of the TiO_2 NTAs, revealing uniform NTAs with an inner diameter of 100 nm and wall thickness of 10–15 nm. The side-view SEM image in Figure 1b discloses a uniform length of 7 μm for anatase-TiO_2 NTAs. After chemical lithiation in LiOH and annealing in air, the NTAs morph into a beaded film comprising BLTO NPs, as shown in Figures 1c and 1d. The high-resolution SEM image (inset in Figure 1c) shows that the LTO NPs have a spinel-like polyhedral morphology with a size of 100–150 nm. The side-view SEM image discloses that the BLTO NPs are vertically aligned on the Ti foil with a similar length as the pristine NTAs. The transmission electron microscopy (TEM) image (Figure 1e) reveals interconnected NPs with a size of 100–150 nm and a beaded stream-like morphology. The X-ray diffraction (XRD) pattern of BLTO NPs can be indexed to spinel LTO (JCPDS No. 49-0207), except for the peaks from metallic Ti. No residues or parasitic TiO_2 phases can be observed, implying that the TiO_2 is completely converted into spinel LTO after chemical lithiation and annealing. The high-resolution TEM (HR-TEM) image in the inset of Figure 1e shows lattice fringes with a spacing of 0.48 nm, corresponding to the (111) plane of spinel LTO, confirming the high crystallinity of LTO NPs. The high-resolution X-ray photoelectron spectroscopy (XPS) spectrum reveals two broad peaks at 464.1 and 458.4 eV, corresponding to Ti $2p_{1/2}$ and Ti $2p_{3/2}$ of Ti^{4+} in LTO (Fig-

ure S1).[20,21] The mass of the BLTO NPs film with an area of 1 cm^2 and thickness of 7 μm is 1.25 mg, giving a tap density of 1.78 $g\,cm^{-3}$. As the density of the pure LTO phase is 3.42 $g\,cm^{-3}$, the overall packing factor of the BLTO NPs film is calculated to be about 0.52, which is larger than that of previously reported LTO.[8,22] The large overall packing factor yields a large battery capacity/weight ratio and volumetric capacity, which bodes well for many applications.

The formation mechanism of BLTO NPs is schematically illustrated in Figure S2, and Figure S3 reveals the morphology evolution process of TiO_2 NTAs to a beaded stream-like film. TiO_2 nanotubes first dissolve in the alkaline solution, forming $[Ti(OH)_6]^{2-}$ that reacts with Li^+ to form LTO, which preferentially nucleates and recrystallizes along the pristine TiO_2 nanotubes, resulting in the formation of heterostructured NP/nanotube composites (Figure S3).[23–25] As the reaction proceeds, the LTO gradually morphs into 3D beaded and stream-like LTO NPs arrays with the TiO_2 nanotubes as the self-sacrificed template. The BLTO NPs film is in direct contact with the underlying metal collector, allowing effective electron transfer from Ti to the BLTO NPs, and vice versa. After repeated bending, the BLTO NPs film directly grown on Ti foil does not break and still adheres to the underlying Ti foil, demonstrating a robust structure as well as excellent adhesion properties and mechanical flexibility (Figure S4).

The electrochemical performance of the BLTO NPs was evaluated by assembling 2032 coin cells with a Li foil as the counter electrode. Figure 2a shows the cyclic voltammetry (CV) curves of the BLTO NPs electrode at a scan rate of 0.1 $mV\,s^{-1}$ in the voltage range between 1 and 2.5 V (vs. Li/Li^+). There are two well-defined redox peaks at 1.65/1.50 V arising from the redox reaction of Ti^{4+}/Ti^{3+}, which is associated with fast lithium insertion/extraction in the spinel LTO lattice.[3,26] The cathodic peaks in the first cycle are slightly biased and the peak area of first cycle is smaller than those of the 2nd or 5th cycles, owing to the incomplete reaction of fresh LTO and side reactions of the electrode.[27] After the 2nd cycle, the peaks in the CV curve almost overlap, indicating a highly reversible reaction in the Li^+ insertion/extraction process. The initial galvanostatic charge/discharge (GCD) profiles acquired at a current density of 50 $mA\,cm^{-3}$ are shown in Figure 2b, which show two obvious and large plateaus with a narrow gap of about 30 mV, indicating small polar resistance during Li^+ insertion/extraction. The first GCD capacities are 314 and 274 $mAh\,cm^{-3}$, respectively, showing a high first coulombic efficiency of 87.3%. We also compare the electrochemical properties of BLTO NPs on the Ti current collector with pure LTO nanoparticles synthesized by using a hydrothermal method; the self-supporting and binder-free BLTO NPs film on the Ti support exhibits a much higher capacity than the pure LTO NPs electrode prepared by mixing the active material with conductive carbon and binder (Figure S5). The GCD curves of the self-supporting BLTO NPs film at different current rates from 50 to 5000 $mA\,cm^{-3}$ are depicted in Figure S6. The narrow gap between the GCD potentials leads to fast electron transfer and high rate capability, as shown in Figure 2c. At a low current density of 50 $mA\,cm^{-3}$, the BLTO NPs film exhibits reversible volumetric capacities of

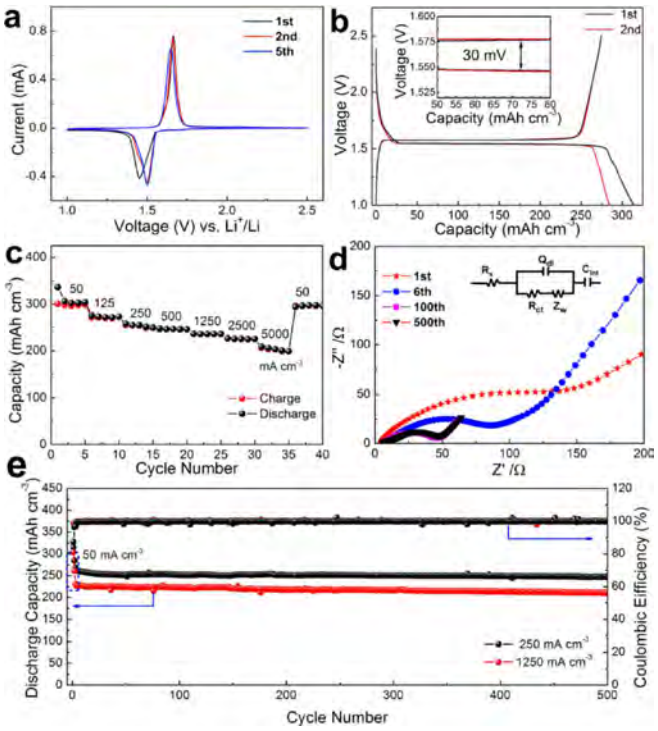

Figure 2. Electrochemical performance of BLTO NPs: a) CV curves of BLTO NPs film at a scan rate of 0.1 $mV\,s^{-1}$; b) GCD profiles of BLTO NPs film at a rate of 50 $mA\,cm^{-3}$; c) GCD capacity of BLTO NPs film at different current rates; d) Nyquist plots of BLTO NPs film. e) Specific capacity and coulombic efficiency of BLTO NPs for 500 cycles at rates of 250 and 1250 $mA\,cm^{-3}$.

304 and about 170 $mAh\,g^{-1}$ based on the mass loading of the BLTO NPs. When the current densities are increased to 125, 250, 500, 1250, and 2500 $mA\,cm^{-3}$, the reversible capacities are 276, 257, 247, 236, and 226 $mAh\,cm^{-3}$, respectively. At a larger rate of 5000 $mA\,cm^{-3}$, the film electrode of BLTO NPs still delivers a capacity of 208 $mAh\,cm^{-3}$, which is about 68.5% of that at 50 $mA\,cm^{-3}$. Moreover, the capacity can be recovered when the current density is reverted back to 50 $mA\,cm^{-3}$, suggesting excellent reversibility. We compared the capacity properties of BLTO NPs with the previously reported LTO-based anodes in the literature, and the self-supporting BLTO NPs film exhibited a much larger capacity and better rate capability. (Figure S7).

Figure 2d shows the electrochemical impedance spectroscopy (EIS) results of the BLTO NPs electrode after different cycles in the frequency range between 100 kHz and 0.1 Hz. All of the EIS plots can be fitted by the equivalent circuit described in the inset of Figure 2d, in which R_s is the electrolyte resistance, the semicircle in the medium-frequency region is the charge-transfer impedance (R_{ct}) including electrode/electrolyte interface resistance and contact resistance of the collector,[28–30] and Z_W and C_{int} represent the Warburg impedance and intercalation capacitance, respectively. As shown in Table S1, the R_{ct} values of the 1st, 6th, and 100th cycles are 129.7, 80.9, and 39.6 Ω, respectively, which shows a noticeable reduction with cycle number, possibly owing to the introduction of the metallic $Li_7Ti_5O_{12}$ phase and the improved electrolyte wettability. This phenomenon is also observed in other LTO anode materials.[27,31–33] The impedance plots after 100 and 500 cycles exhib-

it similar R_{ct} values of 39.6 and 41.1 Ω, respectively, which are smaller than those of LTO-based electrodes reported previously,[34–36] because of the good electrical contact between the current collector and BLTO NPs for electrons transfer. The diffusion coefficient of Li ions (D_{Li}^+) can also be calculated according to Equation (1):[20,36]

$$D_{Li^+} = \frac{1}{2}\left[\left(\frac{V_m}{AF\sigma_w}\right)\frac{dE}{dx}\right]^2 \quad (1)$$

where V_m is the molar volume of LTO (45.73 $cm^3 mol^{-1}$), F is the Faraday constant (96 486 $C mol^{-1}$), A is the total contact area between the electrolyte and the electrode (cm^2), dE/dx is the slope of the open-circuit voltage versus mobile Li^+ concentration x, and the σ_w values at different voltages can be obtained from the slope of Z' versus. $\omega^{-1/2}$ in the Warburg region (Figure S8). The Warburg impedance coefficient (σ_w) and diffusion coefficient of Li ions (D_{Li}^+) were calculated by using Equation (2) and the values are listed in Table S2. D_{Li}^+ is 1.12×10^{-8} $cm^2 s^{-1}$ in the 100th cycle, which is comparable to, or even higher than, those in most literature reports (Table S2), owing to the fact that 3D BLTO NPs provide channels and short diffusion distances for the Li ions.

$$Z' = R + \sigma_w \omega^{-1/2} \quad (2)$$

The long-term cycling performance of the BLTO NPs and corresponding coulombic efficiency at 250 and 1250 mA cm^{-3} are presented in Figure 2e. After 500 cycles at 250 mA cm^{-3}, the capacity loss is only 7.5%, implying 0.015% capacity loss per cycle. At a large current density of 1250 mA cm^{-3}, the capacity is still 225 mAh cm^{-3} after 500 cycles, or 91.4% of the initial capacity, thereby demonstrating high reversibility and cycling stability. The coulombic efficiency is approximately 100% at 250 and 1250 mA cm^{-3}. The superior electrochemical performance can be attributed to the high structural stability of the 3D BLTO NPs and effective electron and ion transport. After 500 cycles, the cell was disassembled and the BLTO NPs were examined by using SEM. Figure 3 shows that, after 500 cycles the film morphology does not change, suggesting excellent durability.

In summary, a self-supporting film comprising BLTO NPs fabricated hydrothermally on a Ti foil in a LiOH solution followed by calcination in air is presented. The 1D TiO_2 nanotubes are fully converted into 1D beaded and stream-like interconnected LTO NPs with a diameter of 100–150 nm. The BLTO NPs provide the diffusion paths for ions and electrons, consequently enhancing the intercalation kinetics in addition to the small contact resistance. Owing to the robust structure and effective electrons transfer, the binder-free BLTO NPs exhibit an excellent rate capability with 68.5% reversible capacity retention when the the current density is increased 100 fold from 50 to 5000 mA cm^{-3}, together with remarkable cycling performance (only 7.5 and 8.6% capacity decay at 250 and 1250 mA cm^{-3} after 500 cycles, respectively). The excellent results suggest potential applications of the BLTO NPs as anodes in next-generation LIBs.

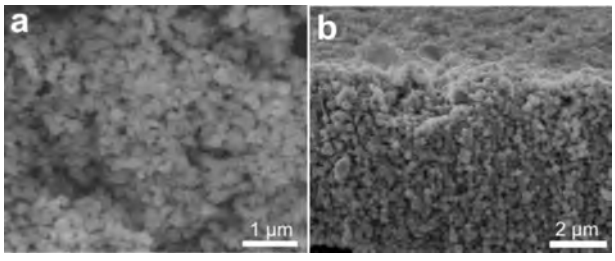

Figure 3. Top-view (a) and side-view (b) SEM images of BLTO NPs film after 500 cycles at a charging/discharging rate of 1250 mA cm^{-3}.

Experimental Section

Materials Synthesis

The Ti foils (1×2 cm^2) were polished by using SiC sandpaper and ultrasonically cleaned with acetone, ethanol, and deionized water sequentially. Anodization was carried out on a conventional two-electrode cell equipped with a direct current (DC) power supply (IT6834, ITECH, China) with the Ti and graphite foils serving as the anode and counter electrode, respectively. The electrolyte was composed of ethylene glycol containing 0.5 wt% ammonium fluoride (NH_4F), 5 vol% distilled water, and 5 vol% methanol (CH_3OH). After anodization at 60 V for 0.5 h, amorphous TiO_2 NTAs were formed on the Ti foil. The sample was ultrasonically cleaned and annealed at 450 °C in air for 3 h to convert the amorphous TiO_2 NTAs into anatase-TiO_2 NTAs.

The self-supporting BLTO NPs film was fabricated on a Ti foil through chemical lithiation and subsequent annealing in air. Typically, the Ti foil covered with anatase-TiO_2 NTAs was immersed in a 0.8 M LiOH solution at 100 °C for 12 h in the Teflon-lined stainless-steel autoclave. After rinsing with distilled water and vacuum drying at 80 °C, the sample was thermally treated at 700 °C in air for 3 h to obtain the self-supporting BLTO NPs film. The pure LTO particles without a Ti support were prepared by using a hydrothermal method.[37] In a typical synthesis, P25 powder (0.4 g) was dispersed in aqueous LiOH solution (60 mL, 1.0 g $LiOH{\cdot}H_2O$). After stirring for 10 min, the suspension was transferred into an 80 mL Teflon-lined autoclave and kept at 180 °C for 24 h. The white precipitate was separated by filtration, washed several times with deionized water to remove the excess hydroxides, before drying at 80 °C for 6 h. Subsequently, the white powder was calcined at 700 °C for 3 h in air to obtain the LTO materials.

Characterization

Field-emission SEM (Nova Nano 450, FEI Co. Ltd., Hillsboro, OR), HR-TEM (Titan 60–300 Cs, FEI Co. Ltd.), XRD (X'Pert PRO MPD, Philips Co. Ltd.), and XPS (ESCALB MK-II, VG Instruments Co. Ltd., London, U.K.) were used to characterize the samples.

Electrochemical Measurements

The electrochemical experiments were conducted by using 2032-type coin cells. The coin cell was assembled in an Ar-filled glove box (MBraun Unilab). A metallic lithium foil was used as the anode and Celgard 2400 (Celgard, LLC Corp., USA) as the separator. The electrolyte was composed of 1.0 M $LiPF_6$ in a mixture of ethylene carbonate (EC) and diethyl carbonate (DEC) (volume ratio = 1:1).

The pure LTO particle electrode, without the supporting Ti, were fabricated by using a traditional slurry-coating method. The slurry consisted of 80 wt% active material (pure LTO nanoparticles), 10 wt% acetylene black, and 10 wt% polyvinylidene fluoride (PVDF). Then, the slurry was uniformly spread on a copper foil current collector, which was vacuum dried overnight. The as-obtained film was cut into circular piece with a diameter of 1 cm and assembled in a coin button cell in the same way as the BLTO NPs. GCD was performed on the assembled cells by using a LANDCT2001A system (Wuhan LAND electronics Co. Ltd., China) in the voltage range between 1 and 2.5 V (vs. Li^+/Li). CV was performed on a CHI 760E electrochemical workstation (Shanghai CH Instrument Co., Ltd., China) at a scanning rate of 0.1 $mV s^{-1}$ in the potential range of 1–2.5 V (vs. Li/Li^+). EIS was conducted in the frequency range between 0.1 Hz and 100 KHz on the CHI 760E electrochemical workstation. All electrochemical measurements were carried out at room temperature.

Acknowledgements

This work was financially supported by the National Natural Science Foundation of China (NSFC; grant nos.: 51572100, 51504171 and 31500783), Natural Science Foundation of Hubei Province (2015CFA116), Fundamental Research Funds for the Central Universities (HUST: 0118 187099), Project of Hubei Provincial Education Office (B2015346), Outstanding Young and Middle-aged Scientific Innovation Team of Colleges and Universities of Hubei Province (T201402), and City University of Hong Kong Applied Research Grant (ARG; No. 9667104). The authors are grateful for the facilities provided by the Analytical and Testing Center of HUST.

Keywords: anode · binder-free film · $Li_4Ti_5O_{12}$ · lithium-ion batteries · nanoparticles

[1] M. Armand, J. M. Tarascon, *Nature* **2008**, *451*, 652 – 657.
[2] Y. X. Tang, Y. Y. Zhang, W. L. Li, B. Ma, X. D. Chen, *Chem. Soc. Rev.* **2015**, *44*, 5926 – 5940.
[3] L. F. Shen, X. G. Zhang, E. Uchaker, C. Z. Yuan, G. Z. Cao, *Adv. Energy Mater.* **2012**, *2*, 691 – 698.
[4] G. N. Zhu, Y. G. Wang, Y. Y. Xia, *Energy Environ. Sci.* **2012**, *5*, 6652 – 6667.
[5] A. D. Roberts, X. Li, H. F. Zhang, *Chem. Soc. Rev.* **2014**, *43*, 4341 – 4356.
[6] N. S. Choi, Z. H. Chen, S. A. Freunberger, X. L. Ji, Y. K. Sun, K. Amine, G. Yushin, L. F. Nazar, J. Cho, P. G. Bruce, *Angew. Chem. Int. Ed.* **2012**, *51*, 9994 – 10024; *Angew. Chem.* **2012**, *124*, 10134 – 10166.
[7] J. Y. Liao, V. Chabot, M. Gu, C. M. Wang, X. C. Xiao, Z. W. Chen, *Nano Energy* **2014**, *9*, 383 – 391.
[8] S. Chen, Y. L. Xin, Y. Y. Zhou, Y. R. Ma, H. H. Zhou, L. M. Qi, *Energy Environ. Sci.* **2014**, *7*, 1924 – 1930.
[9] X. C. Sun, P. V. Radovanovic, B. Cui, *New J. Chem.* **2015**, *39*, 38 – 63.
[10] L. Ye, Q. H. Liang, Y. Lei, X. L. Yu, C. P. Han, W. C. Shen, Zheng.H Huang, F. Y. Kang, Q. H. Yang, *J. Power Sources* **2015**, *282*, 174 – 178.
[11] T. F. Yi, S. Y. Yang, Y. Xie, *J. Mater. Chem. A* **2015**, *3*, 5750 – 5777.
[12] L. Sun, J. P. Wang, K. L. Jiang, S. S. Fa, *J. Power Sources* **2014**, *248*, 265 – 272.
[13] C. F. Lin, X. Y. Fan, Y. L. Xin, F. Q. Cheng, M. O. Lai, H. H. Zhou, L. Lu, *J. Mater. Chem. A* **2014**, *2*, 9982 – 9993.
[14] M. R. Jo, Y. S. Jung, Y. M. Kang, *Nanoscale* **2012**, *4*, 6870 – 6875.
[15] G. B. Xu, W. Li, L. W. Yang, X. L. Wei, J. W. Din, J. X. Zhong, P. K. Chu, *J. Power Sources* **2015**, *276*, 247 – 254.
[16] G. N. Zhu, H. J. Liu, J. H. Zhuang, C. X. Wang, Y. G. Wang, Y. Y. Xia, *Energy Environ. Sci.* **2011**, *4*, 4016 – 4022.
[17] L. F. Shen, E. Uchaker, X. G. Zhang, G. Z. Cao, *Adv. Mater.* **2012**, *24*, 6502 – 6506.
[18] B. L. Ellis, P. Knauth, T. Djenizian, *Adv. Mater.* **2014**, *26*, 3368 – 3397.
[19] J. Liu, K. P. Song, P. A. van Aken, J. Maier, Y. Yu, *Nano Lett.* **2014**, *14*, 2597 – 2603.
[20] M. Guo, S. Q. Wang, L. X. Ding, L. Zheng, H. H. Wang, *J. Mater. Chem. A* **2015**, *3*, 10753 – 10761.
[21] J. P. Yue, C. Suchomski, T. Brezesinski, B. M. Smarsly, *ChemNanoMat* **2015**, *1*, 415 – 421.
[22] N. A. Kyerematen, T. M. Dinh, D. Pech, *RSC Adv.* **2015**, *5*, 61502 – 61507.
[23] X. M. Zhang, K. F. Huo, L. S. Hu, Z. W. Wu, P. K. Chu, *J. Am. Ceram. Soc.* **2010**, *93*, 2771 – 2778.
[24] K. F. Huo, H. R. Wang, X. M. Zhang, Y. Cao, P. K. Chu, *ChemPlusChem* **2012**, *77*, 323 – 329.
[25] X. M. Zhang, B. Gao, L. S. Hu, L. M. Li, W. H. Jin, K. F. Huo, P. K. Chu, *Cryst-EngComm* **2014**, *16*, 10280 – 10285.
[26] Y. F. Tang, L. Yang, S. H. Fang, Z. Qiu, *Electrochim. Acta* **2009**, *54*, 6244 – 6249.
[27] X. L. Jia, Y. F. Lu, F. Wei, *Nano Res.* **2016**, *9*, 230 – 239.
[28] H. S. Li, L. F. Shen, K. B. Yin, J. Ji, J. Wang, X. Y. Wang, X. G. Zhang, *J. Mater. Chem. A* **2013**, *1*, 7270 – 7276.
[29] H. Han, T. Song, E. K. Lee, A. Devadoss, Y. Jeon, J. Ha, Y. C. Chung, Y. M. Choi, Y. G. Jung, U. Paik, *ACS Nano* **2012**, *6*, 8308 – 8315.
[30] Y. Ding, G. R. Li, C. W. Xiao, X. P. Gao, *Electrochim. Acta* **2013**, *102*, 282 – 289.
[31] M. S. Song, A. Benayad, Y. M. Choi, K. S. Park, *Chem. Commun.* **2012**, *48*, 516 – 518.
[32] D. Young, A. Ransil, R. Amin, Z. Li, Y. M. Chiang, *Adv. Energy Mater.* **2013**, *3*, 1125 – 1129.
[33] Y. J. Sha, X. M. Xu, L. Li, R. Cai, Z. P. Shao, *J. Power Sources* **2016**, *314*, 18 – 27.
[34] W. N. Chen, H. Jiang, Y. J. Hu, Y. H. Dai, C. Z. Li, *Chem. Commun.* **2014**, *50*, 8856 – 8859.
[35] X. L. Jia, Y. F. Kan, X. Zhu, G. Q. Ning, Y. F. Lu, F. Wei, *Nano Energy* **2014**, *10*, 344 – 352.
[36] B. Yan, M. S. Li, X. F. Li, Z. M. Bai, J. W. Yang, D. B. Xiong, D. J. Li, *J. Mater. Chem. A* **2015**, *3*, 11773 – 11781.
[37] L. F. Shen, C. Z. Yuan, H. J. Luo, X. G. Zhang, K. Xua, Y. Y. Xia, *J. Mater. Chem.* **2010**, *20*, 6998 – 7004.

Manuscript received: April 26, 2016
Accepted Article published: June 29, 2016
Final Article published: July 28, 2016

CHEMELECTROCHEM

Supporting Information

Self-Supporting and Binder-Free Anode Film Composed of Beaded Stream-Like $Li_4Ti_5O_{12}$ Nanoparticles for High-Performance Lithium-Ion Batteries

Kaifu Huo,*[a] Xingxing Li,[b] Biao Gao,[b] Lei Wang,[a] Qingwei Li,[a] Xiang Peng,[c] Xuming Zhang,[b, c] Jijiang Fu,[b] and Paul K. Chu*[c]

celc_201600215_sm_miscellaneous_information.pdf

Supporting Information

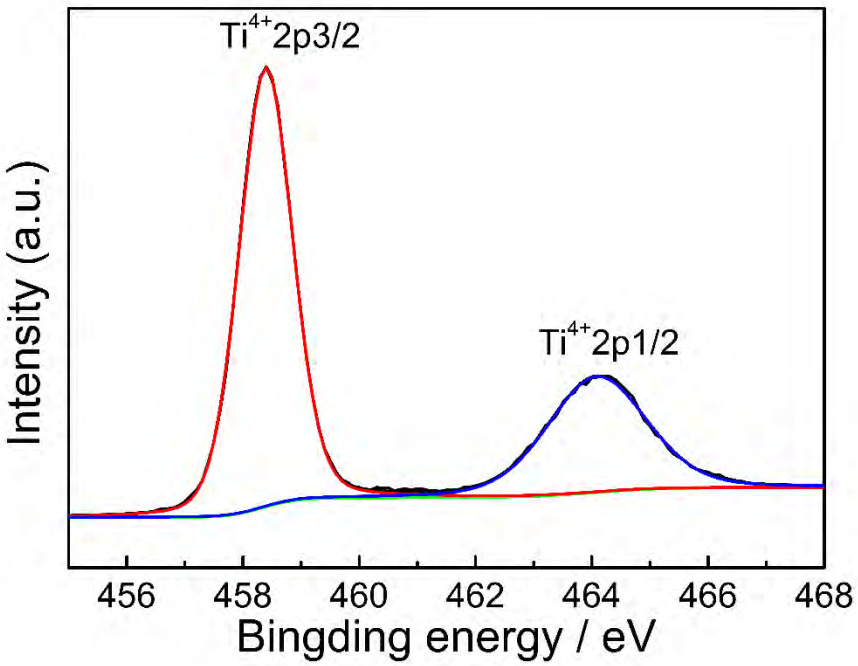

Figure S1. High-resolution XPS spectrum of Ti 2p of BLTO-NPs.

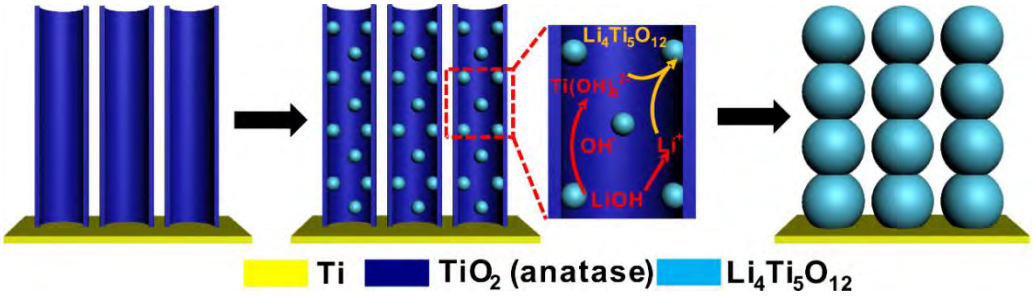

Figure S2. Schematic diagram of the formation process of the BLTO-NPs.

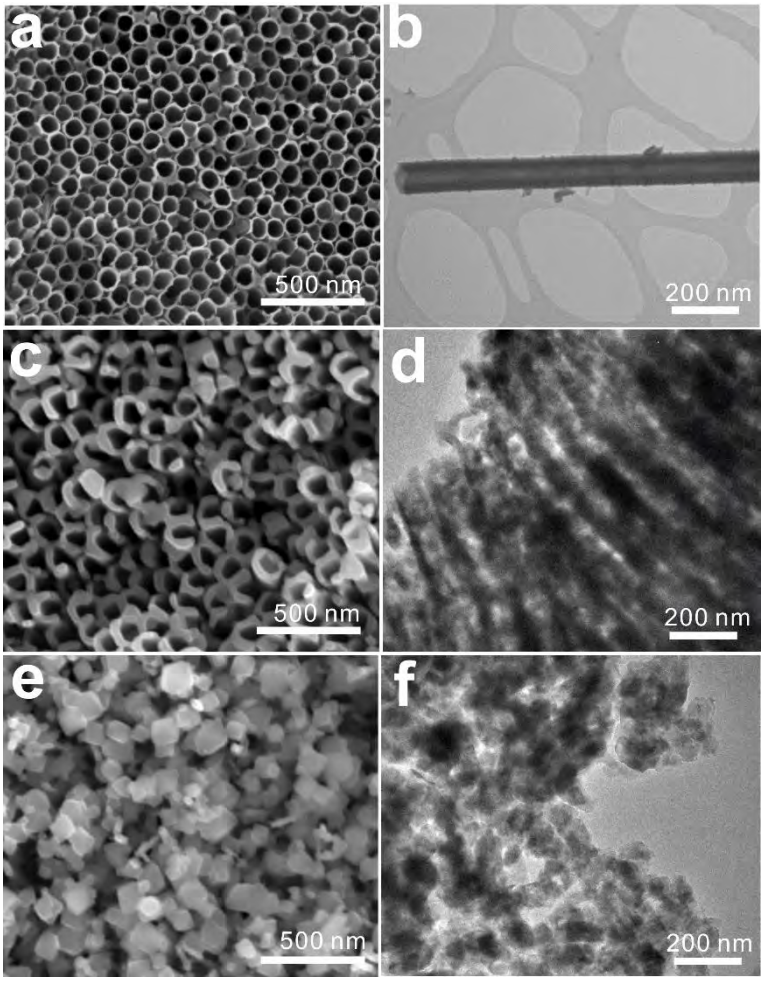

Figure S3. SEM and TEM images of the products for different chemical lithiation durations: (a, b) 0 h, (c, d) 3 h, and (e, f) 6 h.

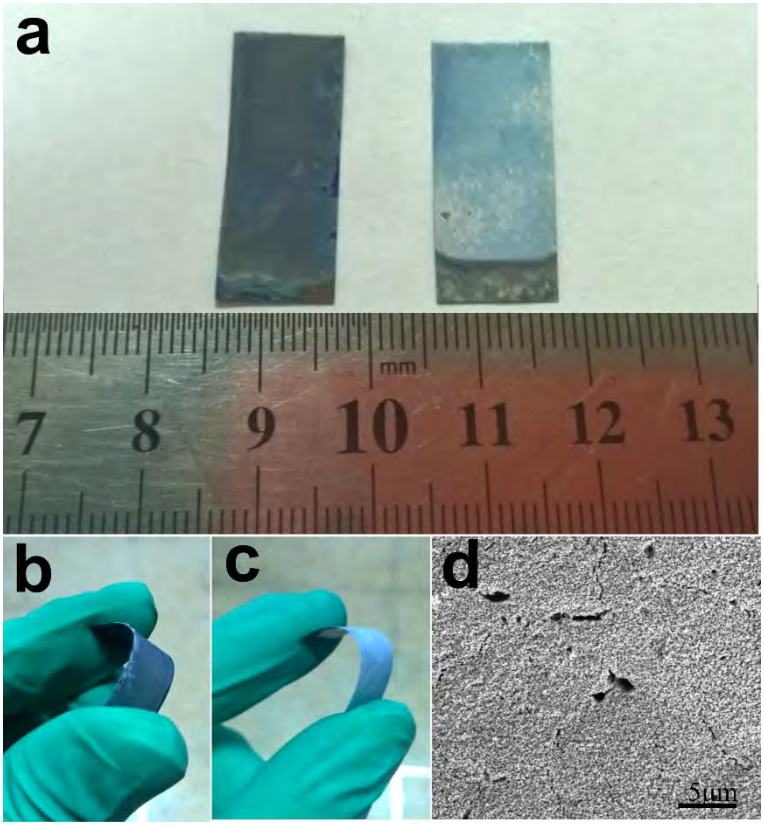

Figure S4. The digital photographs of the surface of anatase TiO_2-NTAs (b) and BLTO-NPs (c) on Ti foils, respectively. (d) SEM micrographs of self-supporting and binder-free BLTO-NPs on the Ti foil after bending.

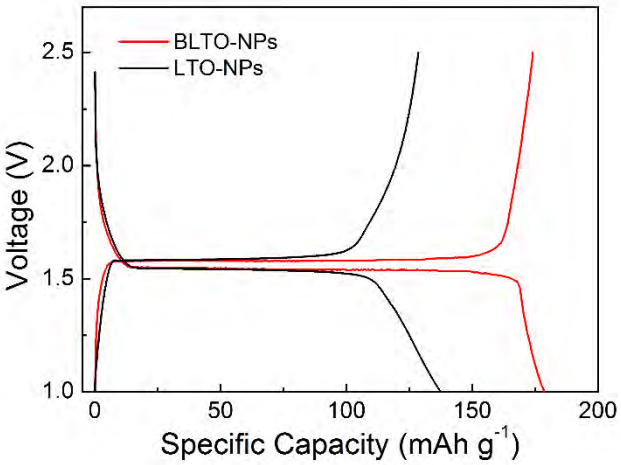

Figure S5. Second GCD curve of the BLTO-NPs and LTO-NPs at the current density of 50 mA cm^{-3} between 1 and 2.5 V.

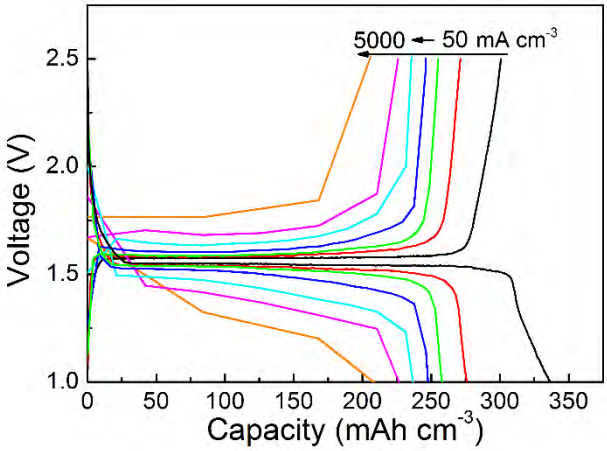

Figure S6. GCD profiles of the BLTO-NPs at different current rates from 50 to 5000 mA cm^{-3}.

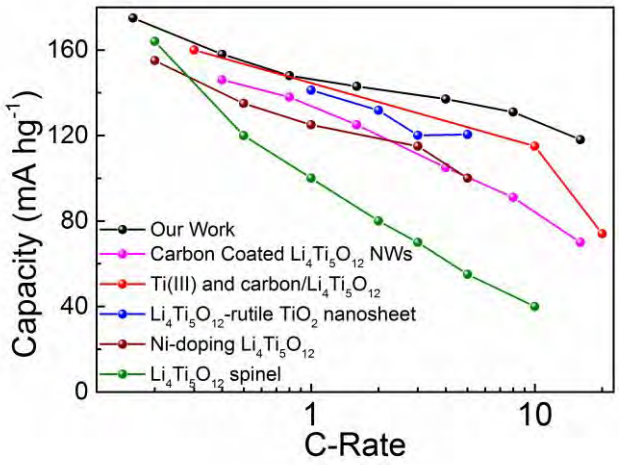

Figure S7. Comparison of rate capability of BLTO-NPs with other reported recently LTO-based electrode prepared by mixing active material with conductive carbon and binder.[1-5]

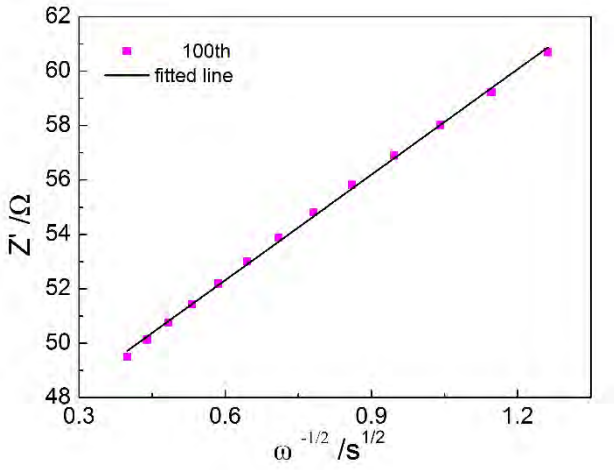

Figure S8 Linear relationship between the real impedance (Z′) and inverse of the square root of the angular frequency ($\omega^{-1/2}$) in the low frequency region for the BLTO-NPs in the 100th cycle.

Table S1. Summary of the impedance parameters of the BLTO-NAs after different cycles

BLTO-NAs	$R_s(\Omega)$	$R_{ct}(\Omega)$
1st	4.19	129.7
6th	9.22	80.89
100th	5.81	39.56
500th	5.66	41.14

Table S2. Comparison of D_{Li}^+ of BLTO-NPs with other LTO-based electrode in the 100th cycle.

D_{Li}^+ ($cm^2\ s^{-1}$)	Ref.
1.12×10^{-8}	Our Work
1.44×10^{-9}	6
2.71×10^{-10}	7
7.19×10^{-9}	8
1.43×10^{-11}	9
5.10×10^{-12}	10
7.97×10^{-12}	11

References:

[1] T.F. Yi, S.Y. Yang, Y.R. Zhu, Y. Xie, R.S. Zhu, *Int. J. Hydrogen Energy* **2015**, *40*, 8571-8578.

[2] Y.G. Wang, H.M. Liu, K.X. Wang, H. Eiji, Y.R. Wang, H.S. Zhou, *J. Mater. Chem.* **2009**, *19*, 6789-6795.

[3] J.Y. Liu, Y. Shen, L. Chen, Y.G. Wang, Y.Y. Xia, *Electrochimica Acta* **2015**, *156*, 38-44.

[4] J. Kim, S.W. Kim, H. Gwon, W.S. Yoon, K. Kang, *Electrochimica Acta* **2009**, *54*, 5914-5918.

[5] A. Mahmoud, J.M. Amarilla, I. Saadoune, *Electrochimica Acta* **2015**, *163*, 213-222.

[6] Y.J. Sha, X.M. Xu, L. Li, R. Cai, Z.P. Shao, *J. Power Sources* **2016**, *314*, 18-27.

[7]M. Guo, S.Q. Wang, L.X. Ding, L. Zheng, H.H. Wang, *J. Mater. Chem. A* **2015**,*3*, 10753-10761.

[8]B. Yan, M.S. Li, X.F. Li, Z.M. Bai, J.W. Yang, D.B. Xiong, D.J. Li, *J. Mater. Chem. A* **2015**, *3*, 11773-11781.

[9] C.C. Chen, Y.A. Huang, H. Zhang, X.F. Wang, G.Y. Li, Y.J. Wang, L.F. Jiao, H.T. Yuan, *J. Power Sources* **2015**, *278*, 693-702.

[10] S.L. Chou, J.Z. Wang, H.K. Liu, S.X. Dou, *J. Phys. Chem. C* **2011**, *115*, 16220-1622.

[11] G.J. Wang, J. Gao, L.J. Fu, N.H. Zhao, Y.P. Wu, T. Takamuraa, *J. Power Sources* **2007**, *174*, 1109-1112.